Int J Adv Manuf Technol (2016) 86:935–942
DOI 10.1007/s00170-015-8163-2

ORIGINAL ARTICLE

Observation and modeling research of high-velocity flushing effect on the performance of BEAM

Fawang Zhang[1] · Lin Gu[1] · Jipeng Chen[1] · Hui Xu[1] · Wansheng Zhao[1]

Received: 3 September 2015 / Accepted: 24 November 2015 / Published online: 30 December 2015

Abstract Blasting erosion arc machining (BEAM) is a novel high efficiency electrical erosion process, which is characterized by a powerful multi-hole inner flushing. In order to study the influence of the high-velocity flushing on the performance of BEAM, a single discharge experiment is carried out on a specially designed observation apparatus, and the phenomena that occurred during the discharge is observed using a high-speed video camera. During the discharge process, a spray cloud of the removed debris near the downstream side of the discharging point is captured by the camera. Tail shaped crater and erosion-corrosion features are also found on the workpiece and electrode surfaces, respectively. These observed phenomena imply that the high-velocity flushing can greatly improve the melting metal removal from the molten pool thereby improving the material removal rate (MRR). For purpose of exploring the mechanism behind, the flow field and pressure distribution of the high-velocity flushing are analyzed by using computational fluid dynamic (CFD) method. The analyzed results indicate that a low-pressure suction effect exists on the downstream side of the electrodes. With the help of the low-pressure suction effect, the high-velocity flushing can continuously take the molten metal out of the molten pool during the discharge, resulting in the reduction of the overheating of the molten metal and improve the efficiency of the discharging energy. Thereby, the work in this paper helps to explain why the high-velocity flushing can markedly promote the material removal rate.

Keywords Blasting erosion arc machining (BEAM) · Single discharge · Arc plasma · High-velocity flushing · Low-pressure suction effect

1 Introduction

Electrical discharge machining (EDM) is able to remove conductive materials by thermal effect regardless of their hardness, and is widely used in the machining of molds, dies, and aerospace parts [1, 2]. But it is badly restricted for application by the comparatively low material removal rate (MRR), especially when used for the machining of high-temperature alloy, such as titanium alloy and nickel-based alloy. In order to overcome this restriction and improve the MRR of conventional EDM, scholars and experts have made many specific research and many achievements have come out [3]. Meshcheriakov et al. [4] found that the controlled arc discharge could attain high MRR and low electrode wear and presented an arc dimensional machining (ADM) method. Han et al. [5] proposed a high-speed EDM milling method which employed moving electric arcs generated with moving electrodes to remove materials. The experimental results showed that the MRR was almost four times greater than that of conventional EDM. Yuan et al. [6] proposed the high-speed electro-erosion milling (HSEM) method aimed to machine the nickel-based alloy efficiently. The HSEM employed a spinning hollow cylindrical tool electrode to let the conductive electrolyte flush into the discharge gap and the workpiece material was removed in the way of milling. Zhao et al. [7] proposed a new type of

✉ Fawang Zhang
zws@sjtu.edu.cn

✉ Lin Gu
lgu@sjtu.edu.cn

[1] State Key Laboratory of Mechanical System and Vibration, School of Mechanical Engineering, Shanghai Jiao Tong University, Shanghai 200240, China

high efficiency material removal process named blasting erosion arc machining (BEAM) based on the hydrodynamic arc breaking mechanism. The investigation showed that the MRR is about 14,000 mm^3/min when machine nickel-based alloy GH4169 using BEAM in the case of sinking model. Meanwhile, the minimum tool wear ratio was less than 1 %. Wang et al. [8, 9] reported that both rough and finish machining could be performed on the same machine by combining traditional EDM with high-speed arc discharge milling. Recent research showed that a high efficiency and greatly improving machined surface integrity could be achieved by combining negative tool polarity and positive tool polarity BEAM [10].

In arc machining process, MRR mainly depends on the machining energy, especially the peak current. However, a large peak current will cause unstable discharging due to the accumulation of heat and debris particles in the working gap [11, 12]. To ensure machining stability and increase machining efficiency, researchers proposed various methods to improve flushing effect in the working gap. Electrode jump flushing can be used to improve discharging stability but it also reduces total effective discharge machining time [13–15], which is bad for the MRR increase. Side jet flushing promotion decreases dramatically from the peripheral region to the central region of the electrode and is only effective in the limited peripheral area [16]. The flushing effect of mono-hole inner flushing is limited by the dimension and the quantity of the hole. So only small or medium peak currents can be applied [17–19]. For purpose of enhancing flushing effectiveness and improving machining efficiency, Zhao and Gu [20] put forward a new type EDM with a bundled electrode. As shown in Fig. 1, the multi-hole electrode produces a high-efficiency flushing named multi-hole inner flushing and therefore high peak current can be applied. Further experimental results showed that comparing with EDM with mono-hole inner flushing, EDM with multi-hole inner flushing produced higher MRR when machining Ti6Al4V [21]. Li et al. [22] discussed that in the multi-hole flushing EDM, the flow velocity increased gradually from the center of the working region to the periphery. Therefore, the powerful multi-hole flushing not only cool down the working gap but also flush the debris away effectively. Thereby, the machining is stable even the peak current is rather high. With the purpose of getting an in-depth study of the influence of high-velocity flushing on BEAM performance, this paper investigated the discharging phenomena using a high-speed video camera during the single discharge experiments conducted on a specially designed observation apparatus. Furthermore, the flow field of the experimental setup was simulated using the ANSYS FLUENT CFD software. The observation and simulation results explain the behind mechanism of the high-velocity flushing improving the machining stability and MRR of BEAM.

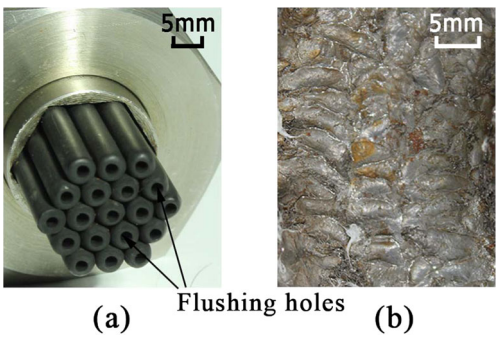

Fig. 1 Bundled electrode (**a**) and machined surface on workpiece (**b**)

2 Experimental setup

In the BEAM process, the phenomena can hardly be observed because of the splashing of working liquid and the intense arc blasting. Furthermore, the blazing debris carried by the high-velocity working liquid can damage the camera. Therefore, the experiments were performed on a single discharge experimental setup which was specifically designed and built for observing the phenomena that occurred in the discharge. As shown in Fig. 2, the setup consists of three functional subsystems: flushing subsystem, electrical subsystem, and observing subsystem. The flushing subsystem consists of a pump, a dielectric tank, and some control valves. It is used to provide a controllable powerful dielectric flushing. In the electrical subsystem, a pulse generator and control switches are used to supply the discharge energy. An oscilloscope with a current sensor and a voltage probe is used to monitor the peak current and voltage during the discharge. In the observing subsystem, a pair of needle-plate electrodes is installed in an

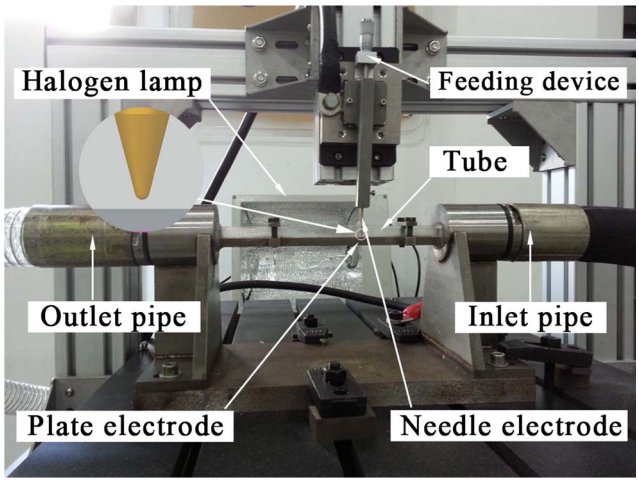

Fig. 2 Experimental setup

Table 1 Single discharge experimental parameters

Needle polarity	Negative
Dielectric	Water
Gap distance, μm	50
Open voltage, V	90
Peak current, A	100, 200, 300
Pulse duration, ms	2, 5, 10
Flushing velocity, m/s	7
Frame frequency, fps	5000

$8 \times 8 \times 150$ mm^3 transparent duct which bridges the inlet and outlet pipes and lets the controllable powerful dielectric flushing pass through. A die steel plate serves as the plate electrode and a 2.5-mm-diameter copper cylinder with a sharp tip mounted on a feeding device serves as the needle electrode. The gap between the electrodes is controlled by the feeding device. The MotionPro high-speed video camera made by Integrated Design Tools, Inc. is used to observe and record the phenomena occurred in the discharge. The halogen lamp is employed to provide the backlight.

The single discharge experiments were conducted according to the conditions listed in Table 1. After the experiments, the erosion surfaces of the electrodes were analyzed by using a Zeiss Stemi 2000-C stereomicroscope.

3 Flow field simulation

In order to explore the mechanism behind the observed phenomena, this section focuses on the simulation of the flow field. Firstly, a 3D geometric model of the flushing dielectric is built. Then the viscous model is determined according to the calculated Reynolds number. At last, the flow field is analyzed by using the CFD software ANSYS FLUENT 14.5.

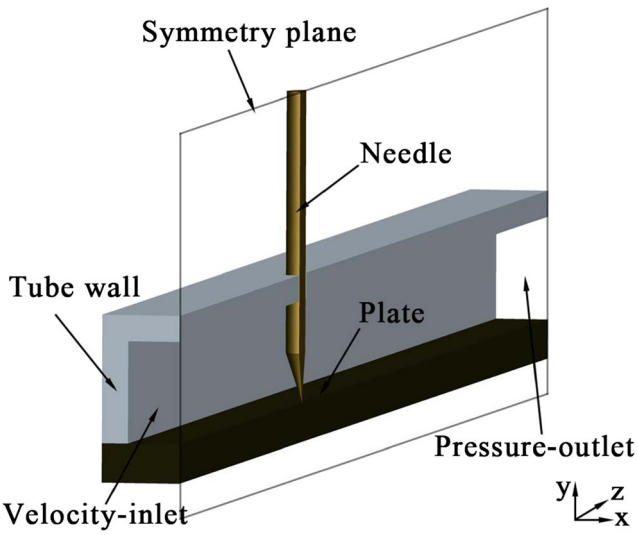

Fig. 3 Geometric model and boundary conditions for analyzing

3.1 Geometric model and boundary conditions

Figure 3 illustrates the geometric model of discharge and flushing apparatus. In the apparatus, a pair of needle-plate electrodes is installed in a duct. The duct size is $8 \times 8 \times 150$ mm^3 which is designed to provide a powerful flushing. According to the measured results in the experiment, the gap distance between the needle and plate electrodes is set as 50 μm. The cavity of the apparatus except for the duct wall and electrodes is the solution domain of the flow field. Since the system is a symmetric object, only 1/2 of the cavity is built in the simulation to reduce the computation burden.

The boundary conditions are also shown in Fig. 3. Inlet velocity and outlet pressure were chosen as inlet and outlet boundary conditions, respectively. Inlet velocity is set to 7 m/s according to the measured result, and outlet pressure is set to 0 Pa, gauge pressure. The default wall condition is accepted for all the rest boundaries. In order to work out the pressure variation in the duct, take outlet as the reference pressure location and set the reference pressure to 101,325 Pa.

3.2 Viscous model

The viscous model is primarily determined according to the Reynolds number which is defined as

$$R_e = \frac{\rho u D}{\mu} \tag{1}$$

where ρ, u, and μ are the density, inlet velocity, and dynamic viscosity, respectively. D is a characteristic linear dimension, and the equivalent value for non-circular cross section pipe is the hydraulic diameter.

The Reynolds number can be calculated by substituting the given value for the variables in Eq. 1 and the calculated result is about 29,000. Therefore, the standard $k-\varepsilon$ viscous model is selected which is valid for fully turbulent flows. In the standard $k-\varepsilon$ viscous model, the turbulence kinetic energy, k, and its rate of dissipation, ε, are obtained from Eqs. 2 and 3.

$$\frac{\partial}{\partial t}(\rho k) + \frac{\partial}{\partial x_i}(\rho k u_i) = \frac{\partial}{\partial x_j}\left[\left(\mu + \frac{\mu_t}{\sigma_k}\right)\frac{\partial k}{\partial x_j}\right] + G_k + G_b - \rho\varepsilon + s_k \tag{2}$$

$$\frac{\partial}{\partial t}(\rho\varepsilon) + \frac{\partial}{\partial x_i}(\rho\varepsilon u_i) = \frac{\partial}{\partial x_j}\left[\left(\mu + \frac{\mu_t}{\sigma_\varepsilon}\right)\frac{\partial \varepsilon}{\partial x_j}\right] + C_{1\varepsilon}\frac{\varepsilon}{k}(G_k + C_{3\varepsilon}G_b) - C_{2\varepsilon}\rho\frac{\varepsilon^2}{k} + s_\varepsilon \tag{3}$$

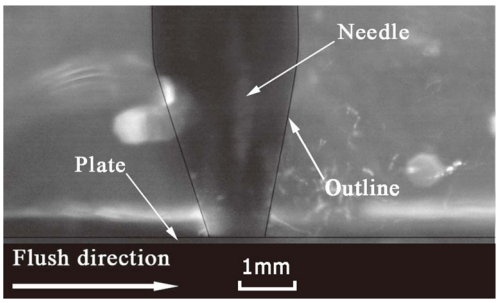

Fig. 4 Photograph before discharging

where, x_i, x_j are the cartesian coordinates, u_i is the velocity component in i-coordinate of the flow. σ_k and σ_ε are the turbulent Prandtl numbers for k and ε, and their values are considered as constants as well as $C_{1\varepsilon}$, $C_{2\varepsilon}$, and $C_{3\varepsilon}$. s_k and s_ε are user-defined source terms and in this model their value are equal to zero for there are no source terms. The turbulent viscosity, μ_t, is computed by

$$\mu_t = \rho C_\mu \frac{k^2}{\varepsilon} \tag{4}$$

where C_μ is a constant. G_b is the generation of turbulence kinetic energy due to buoyancy and its value equals to zero since the temperature gradient and gravity are both negligible. G_k represents the generation of turbulence kinetic energy due to the mean velocity gradients and its value is calculated by

$$G_k = -\rho \overline{\mu_i' \mu_j'} \frac{\partial \mu_j}{\partial x_i} \tag{5}$$

4 Results and discussions

Figure 4 is a photograph captured by the high-speed video camera before discharge. It clearly shows the shapes and locations of the electrodes. But they will be submerged under the strong light of the arc plasma later during the discharge. So their outlines are drawn out aimed to indicate their shapes and relative position in the subsequent analysis.

4.1 Discharge process

According to the different phenomena in obtained pictures, the discharge process of BEAM can be broadly divided into three stages, namely arc striking and expanding stage, debris expelling stage, and arc extinguishing stage. In the arc striking and expanding stage, the discharge channel forms after the dielectric breakdown and then develops into arc. As shown in Fig. 5, the arc strikes at 0.2 ms after the dielectric breakdown on the upstream side of the needle electrode. Then the arc light gradually overgrows the picture at 2.2 ms. It illustrates the expanding process of the discharge channel and this process lasts 2.2 ms. As shown in Fig. 6, the debris expelling stage begins at 2.4 ms and ends at 4.2 ms. During this stage, a spray cloud of the removed debris firstly appears near the working gap on the downstream side. After that, the cloud area and concentrate, which means the quantity of the removed material, initially increases with time increasing and then decreases fast and disappears at 4.2 ms. It indicates that the molten metal expels from the molten pool and forms the debris. Then the debris is diluted and taken away by the flushing dielectric. After the discharge, the filtered debris was analyzed using scanning tunneling microscope (STM). The micrograph of the debris, as shown in Fig. 7, indicates that although the MRR is much lager, the debris size does not increase noticeably compared with the conventional EDM [23] thanks to the powerful flushing. In the last stage, the arc decays gradually and then disappears on the downstream side, as shown in Fig. 8.

4.2 Arc distortion

As mentioned in Section 4.1, the arc strikes on the upstream side of the needle electrode at the beginning of the discharging. On the contrary, the arc goes out on the downstream side of the needle electrode. Based on this phenomenon, it

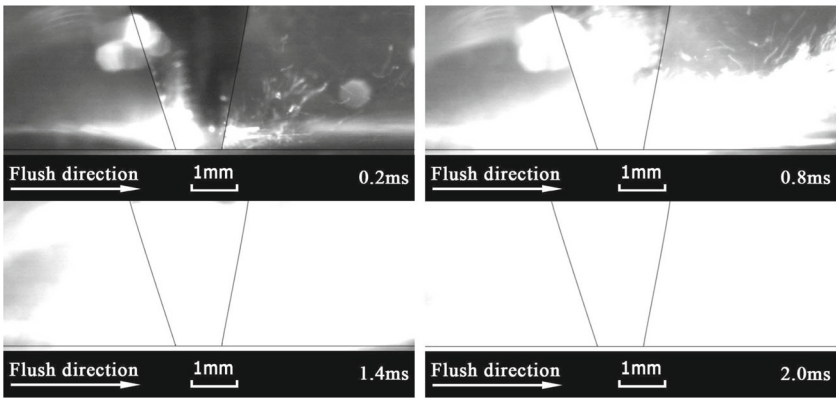

Fig. 5 Arc striking and expanding

Fig. 6 Debris expelling

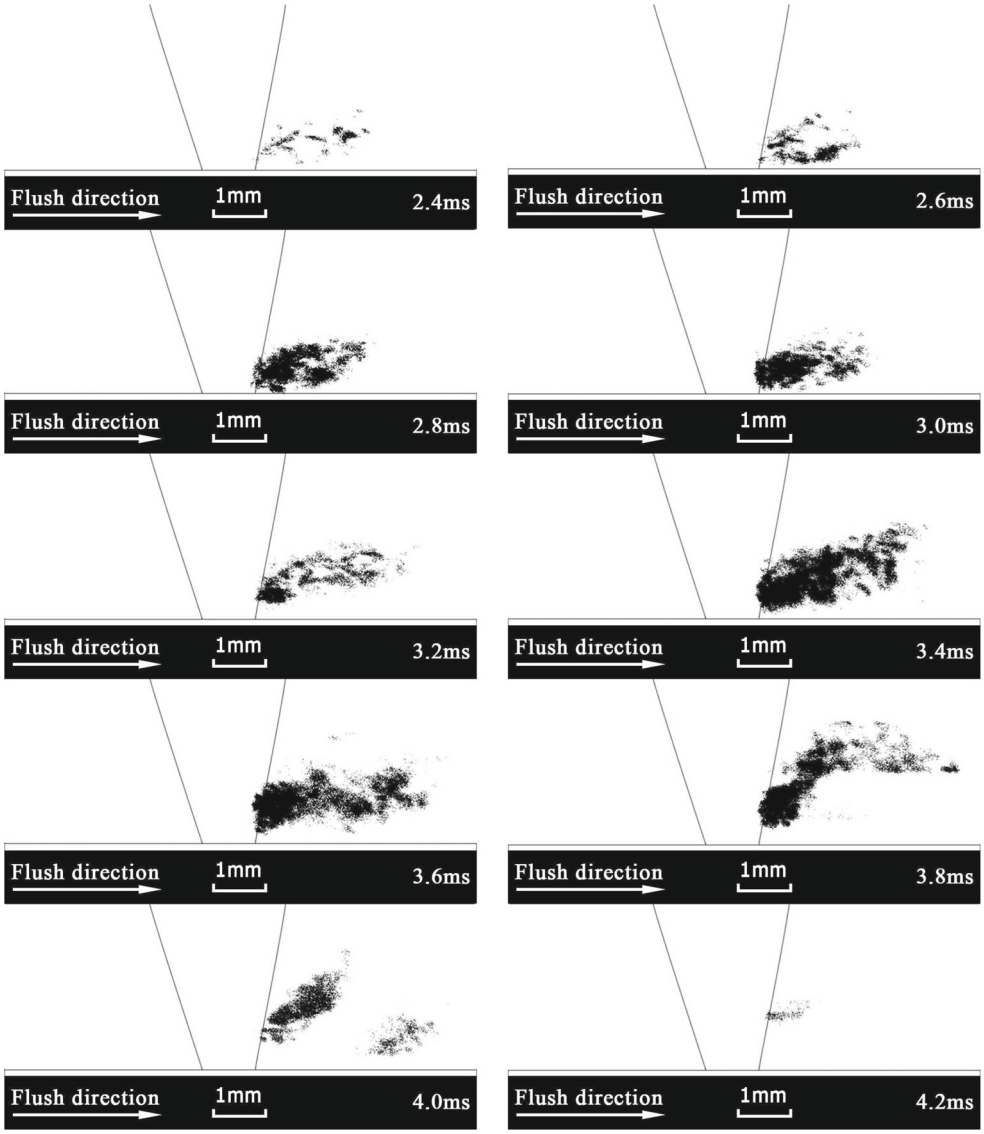

can be inferred that the arc column is distorted by the hydrodynamic force. The distorted arc column moves along the flush direction driven by the hydrodynamic force, resulting in a specific crater with a shallow trailing named tailing crater as shown in Fig. 9a. Due to the moving arc column, the erosion on the needle electrode mainly distributed on the downstream side surface, as shown in Fig. 9b. It should be noted that the flush direction vector in Fig. 9b is perpendicular to the image and points outside.

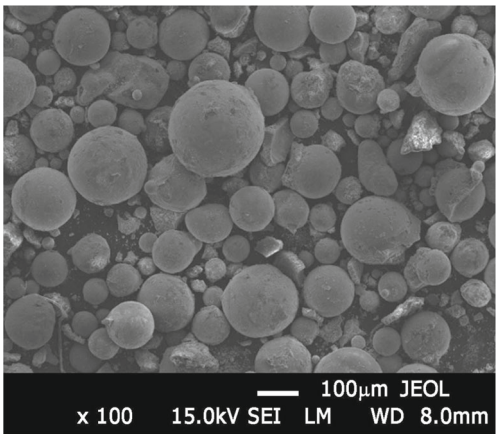

Fig. 7 Micrograph of the debris

4.3 Simulation results

Figure 10 illustrates the simulation results of the dielectric fluid flow field and pressure distribution on the symmetry plane. It should be noted that in the solution domain, the immersed needle electrode is simplified into an equivalent wall and the rest is omitted since only the immersed part involves in the solution. Figure 10a shows that the dielectric sprays out from the working gap in fountain shape on the

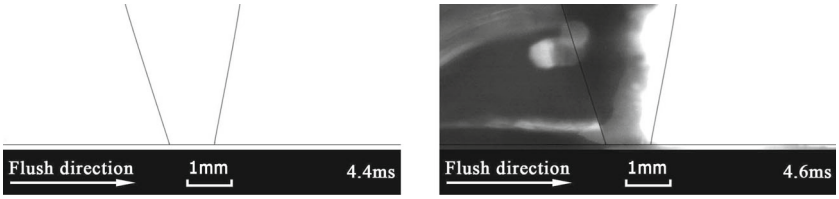

Fig. 8 Arc extinguishing

downstream side when it flows through the needle electrode at a high velocity. This type flow field is very favorable to the process of flushing away the discharge produced debris from the working gap. On the other hand, the contour plot of the pressure distribution indicates that there is a low pressure zone close to the needle electrode on the downstream side, as shown in Fig. 10b.

In order to investigate the pressure distribution, a line through the working gap on the symmetry plane was chosen as the sampling path. Then the curve of pressure versus sampling path is plotted as shown in Fig. 11. It indicates that in the working gap the pressure curve falls steeply to generate a low-pressure zone on the downstream side. The pressure drop reaches a maximum at the tip of the needle electrode. Besides, the simulation results point out that the pressure drop increases with the increasing of the inlet velocity. A significant low-pressure zone exists only when a high enough velocity flushing is applied. So it can be concluded that the high-velocity flushing results in a fountain shape flow velocity distribution and a low-pressure zone on the downstream side of the electrodes.

4.4 Discussions

Evidently, this special fluid field influences the shape and movement of the plasma and then influence the molten metal removal, and this influence is enhanced gradually with the increase of the inlet velocity. What's more, some conclusions can be inferred by associating the simulation results with the experimental results. The metal on the ends of the plasma column was melted rapidly by the high temperature forming a molten pool. Meanwhile, the plasma was distorted by the pressure difference caused by hydrodynamic force and the molten metal was pushed by the

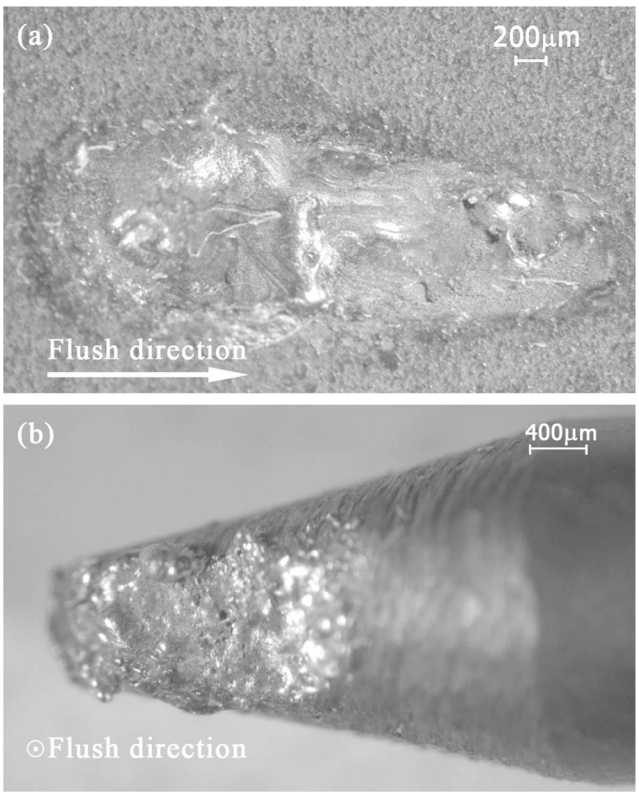

Fig. 9 Micrographs of the erosion surfaces on electrodes. **a** plate electrode; **b** needle electrode

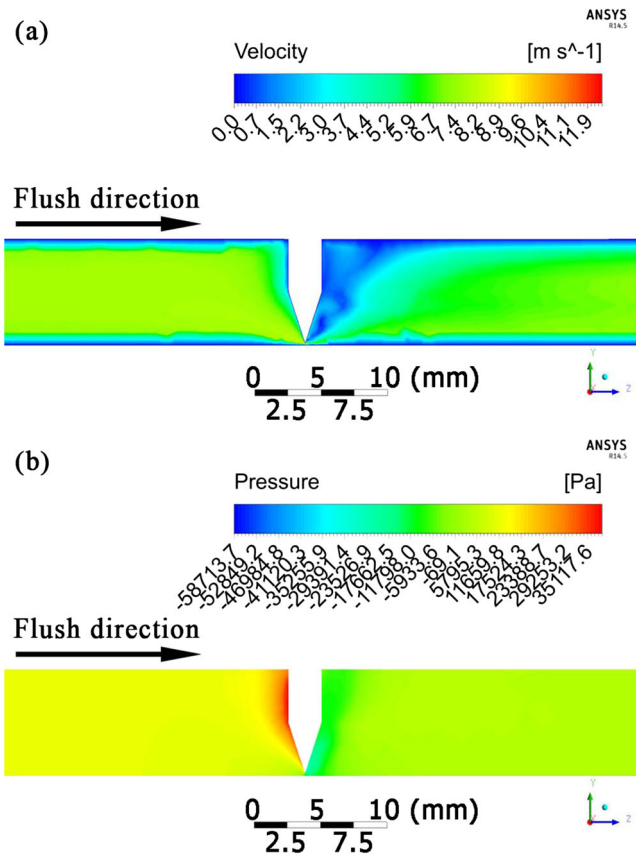

Fig. 10 Simulation results on the symmetry plane. **a** velocity distribution; **b** pressure distribution

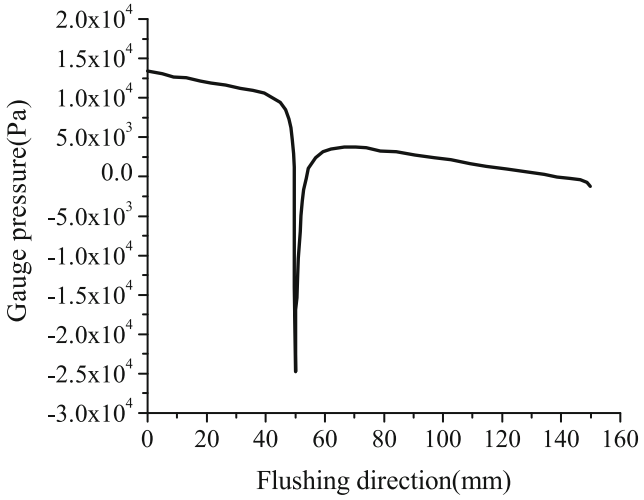

Fig. 11 Pressure distribution along the flushing direction

distorting plasma column into the low-pressure zone on the downstream side of the needle electrode, as described in Section 4.3. Then the big pressure gradient between the molten metal and the low-pressure zone exerted a considerable suction force on the molten metal. As a result, the molten metal was drawn out by the suction force and flushed away by the high-velocity dielectric flushing. Before cooled down, the sprayed molten metal lashed and ablated the needle surface facing to the low-pressure zone on the downstream side. The obtained micrograph of the erosion-corrosion surface caused by the sprayed molten metal is shown in Fig. 9b.

The previous research on conventional EDM shows that the collapse of the plasma yields a strong explosive force at the end of discharge, and the explosive force expels the debris from the molten pool [24–27]. Therefore, the molten metal keeps absorbing heat during the whole discharging process and leads to overheating. Thereby, a large portion of the energy supplied by the pulse generator is consumed as latent heat and taken away for nothing by the debris [28, 29]. However, the high-velocity flushing BEAM is different from the conventional EDM. The low-pressure suction effect caused by the high-velocity flushing enables the molten metal to depart from the molten pool efficiently and timely during the discharge rather than at the end of the discharge. The timely departure of the molten metal dramatically improves the efficiency of discharging energy by reducing the overheating of the molten metal and promotes a large MRR.

5 Conclusions

In this paper, a single discharge experimental setup was specifically designed and built for observing the phenomena occurred in the BEAM discharge. The phenomena occurred during the discharging were captured by a high-speed video camera. According to the different phenomena obtained pictures, the discharge process of BEAM can be broadly divided into three stages: arc striking and expanding stage, debris expelling stage, and arc extinguishing stage.

The flow field and pressure distribution inside the duct were analyzed by using CFD method. The simulated velocity distribution contour plot showed that the dielectric sprayed in fountain shape on the downstream side of the needle electrode when it flowed through at a high speed. Apparently, this velocity distribution benefited the dielectric washing away the debris. The contour plot of the pressure distribution showed that there existed a big pressure difference between the upstream and downstream sides of the needle electrode along the flush direction. It also showed that there existed a low-pressure zone near the downstream side of the needle electrode and the maximum pressure drop increased gradually with the increasing of inlet velocity.

Based on the analyses, a low-pressure suction assisted debris removal mechanism has been suggested and it can be expressed as follow. The pressure difference between the upstream and downstream sides of the tool electrode distorted the plasma column along the flush direction, and the distorting plasma column pushed the molten metal into the low pressure zone. Then the molten metal was drawn out by the suction force and washed away by the high-velocity flushing. The low-pressure suction-assisted debris removal mechanism indicates that a powerful flushing improves the efficiency of discharging energy by reducing the overheating of the molten metal and promotes a large MRR.

Acknowledgements The authors acknowledge the National Natural Science Foundation of China (Grant no. 51235007) and the State Key Laboratory of Mechanical System and Vibration of China (Grant no. MSV201305) for their financial support.

References

1. Abdulkareem S, Khan AA, Konneh M (2009) Int J Adv Manuf Technol 45(11-12):1146
2. Chiang KT (2008) Int J Adv Manuf Technol 37(5-6):523
3. Klocke F, Klink A, Veselovac D, Aspinwall DK, Soo SL, Schmidt M, Schilp J, Levy G, Kruth JP (2014) CIRP Annals-Manufacturing Technology 63(2):703
4. Meshcheriakov G, Nosulenko V, Meshcheriakov N, Bokov V (1988) CIRP Ann-Manuf Techn 37(1):209
5. Han F, Wang Y, Zhou M (2009) International journal of machine tools and manufacture 49(1):20
6. Yuan R, Wei B, Luo Y, Zhan Y, Xu W, Lamphere M (2010) ISEM-16
7. Zhao W, Gu L, Xu H, Li L, Xiang X (2013) Procedia CIRP 6:621
8. Wang F, Liu Y, Tang Z, Ji R, Zhang Y, Shen Y (2013) Proceedings of the Institution of Mechanical Engineers, Part B: Journal of Engineering Manufacture p. 0954405413506194

9. Wang F, Liu Y, Zhang Y, Tang Z, Ji R, Zheng C (2014) J Mater Process Technol 214(3):531
10. Xu H, Gu L, Chen J, Hu J, Zhao W (2015) Int J Adv Manuf Technol:1–11
11. Kunieda M, Yanatori K (1997) IJEM 2:43
12. Schumacher BM (1990) CIRP Ann-Manuf Techn 39(1):197
13. Cetin S, Okada A, Uno Y (2003) J Manuf Sci E-T ASME 125(4):809
14. Cetin S, Okada A, Uno Y (2004) JSME Int J C 47(2):553
15. Masuzawa T, Heuvelman CJ (1983) CIRP Ann-Manuf Techn 32(1):109
16. Masuzawa T, Cui X, Taniguchi N (1983) CIRP Ann-Manuf Techn 41(1):239
17. Koenig W, Weill R, Wertheim R, Julzler WI (1977) CIRP Ann-Manuf Techn 25(1):71
18. Ozgedik A, Cogun C (2005) Int J Adv Manuf Technol 2(5-6):488
19. Wong YS, Lim LC, Lee LC (1995) J Mater Process Technol 48(1):299
20. Zhao WS, Gu L, Li L, Xia YG, Li L (2007) Proceedings of the 15th International Symposium on Electromachining (ISEM 15)(University of Nebraska-Lincoln, Pittsburgh, Pa), pp. 41–44
21. Gu L, Li L, Zhao WS, Rajurkar KP (2012) Int J Mach Tool and Manu 53(1):100
22. Li L, Gu L, Xi XC, Zhao WS (2012) Int J Adv Manuf Technol 58(1-4):187
23. Cabanillas E, Pasqualini E, López M, Cirilo D, Desimoni J, Mercader R (2001) Hyperfine interactions 134(1):179
24. Zolotykh BN (1960) Soviet Physics-Technical Physics 4(12):1370
25. Eubank PT, Patel MR, Barrufet MA, Bozkurt B (1993) J Appl Phys 73(11):7900
26. Yeo SH, Kurnia W, Tan PC, J Phys D (2007) Appl Phys 40(8):2513
27. Tao J, Ni J, Albert JS (2012) J Manuf Sci Eng 134(1):011–002
28. Zahiruddin M, Kunieda M (2010) J Adv Mech Des Syst 4(6):1095
29. Zahiruddin M, Kunieda M (2012) CIRP Ann-Manuf Techn 61(1):187